The MR Cap: A single#sided MRI system designed for potential point#of#care limited field#of#view brain imaging

Citation: McDaniel, Patrick C., Cooley, Clarissa Zimmerman, Stockmann, Jason P. and Wald, Lawrence L. 2019. "The MR Cap: A single#sided MRI system designed for potential point#of# care limited field#of#view brain imaging." Magnetic Resonance in Medicine, 82 (5).

As Published: http://dx.doi.org/10.1002/mrm.27861

Publisher: Wiley

Persistent URL: https://hdl.handle.net/1721.1/141014

Version: Author's final manuscript: final author's manuscript post peer review, without publisher's formatting or copy editing

Published in final edited form as:

Magn Reson Med. 2019 November ; 82(5): 1946–1960. doi:10.1002/mrm.27861.

The MR Cap: a single-sided MRI system designed for potential point-of-care limited field-of-view brain imaging

Patrick C McDaniel[1,2,*], **Clarissa Zimmerman Cooley**[2,3], **Jason P Stockmann**[2,3], **Lawrence L Wald**[2,3,4]

[1]Dept. of Electrical Engineering and Computer Science, Massachusetts Institute of Technology, Cambridge, MA, USA

[2]Athinoula A Martinos Center for Biomedical Imaging, Department of Radiology, Massachusetts General Hospital, Charlestown, MA, USA

[3]Harvard Medical School, Boston, MA, USA

[4]Division of Health Sciences and Technology, Harvard - Massachusetts Institute of Technology, Cambridge, MA, USA

Abstract

Purpose—The size, cost and siting requirements of conventional MRI systems limit their availability and preclude usage as monitoring or point-of-care devices. To address this, we developed a lightweight MRI for point-of-care brain imaging over a reduced FOV.

Methods—The B_0 magnet was designed with a genetic algorithm optimizing homogeneity over a 3×8×8cm FOV and a built-in gradient for slice-selection or readout encoding. An external pair of gradient coils enables phase encoding in the other two directions and an RF coil provides excitation and detection. The system was demonstrated with high resolution 1D "depth profiling" and 3D phantom imaging.

Results—The light-weight B_0 magnet achieved a 64mT average field over the imaging region at a materials cost of under $450 USD. The weight of the magnet, gradient and RF coil was 8.3 kg. Depth profiles were obtained at high resolution (0.89mm) and multi-slice RARE images were obtained with a resolution ~2mm in-plane and ~6mm slice thickness, each in an imaging time of 11 min.

Conclusion—The system demonstrates the feasibility of a lightweight brain MRI system capable of 1D to 3D imaging within a reduced FoV. The proposed system is low-cost and small enough to be used in point-of-care applications.

Keywords

point-of-care; accessible MRI; portable MRI; low-cost MRI

---

[*] Corresponding Author; contact: Patrick C McDaniel, 77 Massachusetts Ave Rm 36-776, Cambridge, MA 02139, USA, patmcd@mit.edu,

Introduction

MRI has become a routine part of clinical medicine, especially for neuroimaging. However, expense, size, and siting requirements impose limitations on how conventional MRI scanners can be used within the health-care system. Installation of a whole-body MR scanner or even a head-only type device using a conventional superconducting magnet entails a dedicated space, special infrastructure and safety requirements, such as a 5-Gauss exclusion area, high-power electrical supply, cooling system and shielded room. These prerequisites preclude the use of MRI in many settings, such as rural or developing-world clinics that might not possess this infrastructure. Furthermore, prior to receiving an MR scan, a patient must undergo a screening process and be moved into the magnet on a specialized patient table. In general, the nature of the full-sized scanner requires the scanner to be operated as a central facility within the healthcare center whereby the patient is brought to the MRI and not vice-versa.

Together these requirements also preclude the use of MRI in time-sensitive situations or intensive-care settings where a patient cannot be transported from the point-of-care setting. The cost and dedicated centralized nature of current MRI facilities also prevents MRI from being used for continuous monitoring of a patient. While the high-quality, versatile but immobile nature of current MRI scanner configurations is well suited to the model with which they are used, it limits the reach of MRI. This paradigm has been successfully extended for other imaging modalities. For example there exist low-cost, portable ultrasound (1–3), CT (4), and gamma camera (5) systems in addition to the permanently sited, more expensive systems in each modality that produce the highest quality images. The mobile variants of these devices do not necessarily generate images of the same caliber as their more expensive counterparts, but their images are diagnostically useful and extend the reach of these modalities. In this work, we present a point-of-care MRI scanner designed to operate in analogy to other low-cost point-of-care modalities. The system has reduced imaging FOV and performance compared to conventional systems, but is vastly cheaper, lighter and more portable, potentially extending the range of MRI to point-of-care applications.

Recent reviews have examined the development of portable and low-cost MRI systems for brain imaging (6,7). These include ultra-low field systems which attempt to reduce cost and weight by reducing B_0 below 10mT (8–10), prepolarized systems (11,12), low field systems employing resistive magnets or permanent magnet arrays, potentially employing built-in encoding fields (7,13–15), and high field systems with reduced cryogen use or new superconductor or cryostat technology (16). Portable MRI systems have also been developed for extremity imaging (17) and have found applications in MSK imaging (18,19). Even smaller and more portable MR systems can be seen in the field of “single-sided” NMR systems (20). These systems have been designed for use in chemical analytics (21,22), petrology (23), and food science (24) and allow the sample under test to be placed in a sensitive region *outside of* the device. Some of these devices, such as the NMR-MOUSE (25), are commercially available. Some studies have explored the use of such ultra-portable “single-sided” spectrometers and relaxometers for medical applications, such as for skin profiling (26), mammographic (27), and hydration monitoring (28,29) applications. These single-sided systems are far smaller than traditional MR scanners where the patient is interior to the magnet and thus have the potential to be true "point-of-care" devices. Prior work has also demonstrated imaging with a single-sided MR magnet (30). The imaging region of this device was 42 × 42 × 10 mm with a steep (2.5 T/m) gradient extending away from the single sided magnet. This steep field drop-off required coil re-tuning at different depths, limited the depth penetration and potentially introducing strong diffusion dephasing. Thus, a larger 3D volumetric sensitive region with a gentler field drop-off is desirable for brain applications.

Here, we describe and test the "MR Cap": a single-sided MRI device for brain imaging over a 3D volume. This system has the form factor of a standard bicycle helmet (Figure 1a), and a sensitive volume that extends 3 cm beneath the scalp and into cerebral cortex when positioned on an adult head (Figure 1b). The MR Cap is light enough (under 10kg) that it could be attached to posable arm (Figure 1a) and then arbitrarily positioned, allowing movement of the sensitive volume to different regions of the brain. This feature might allow the MR Cap to be positioned on the head of a bed-bound subject or to be placed on a subject for an extended time, creating the possibility of point-of-care and continuous-monitoring applications. A preliminary version of this work was previously published in abstract form (31). Potential applications of a point-of-care single sided MR system could include assessment of hemorrhage during emergency or postoperative care or the assessment of cerebral vasculature in large structures such as the sagittal sinus.

Methods

B_0 Magnet design:

The magnet was designed from NdFeB permanent magnets arranged in a "cap-shaped" configuration to be positioned on top of an adult's head. The cap was designed to closely fit an adult head in order to maximize the B_0 field strength. This required the gradient coils to be placed external to the magnet. The magnet has a transverse-oriented B_0 field with an imaging ROI that includes part of the subject's skull and superficial cortex (Figure 2a). This target ROI was chosen to be ~3×8×8cm and to have a lenticular shape whose curved surface roughly matches the shape of the RF loop coil's B_1^- sensitivity profile. Single-sided magnets such as this inevitably have large field gradients moving away from the magnet surface. We use this built-in B_0 gradient for readout or slice select encoding. We took steps in the magnet design to avoid the very strong (>1T/m) gradients found in many single sided MR systems.

The placement of the NdFeB magnet material was chosen using a genetic optimization framework similar to a previous Halbach cylinder design method (32). This process started with a continuous magnet material "cap-shaped" section of an ideal Halbach sphere (33). The continuous magnetization (Figure 2b) was then discretized into 37 blocks (Fig. 2c). This discretized Halbach sphere section is practical to construct and has the desired field orientation, but is not optimized for in-plane homogeneity or gradient strength. To perform this optimization, the genetic algorithm was then allowed to alter the sizes, block magnetization grade and translational positions of each block (Fig. 2d) similar to previous work optimizing a Halbach cylinder (34–36). The positions of the simulated blocks were allowed to vary along x by up to +/−1cm and 6 of the 37 blocks were allowed to move along z by up to +/−1cm during optimization. The composition of each block could take one of either 7 or 9 size/material combinations ranging from a non-magnetic block to an N52-grade block of dimensions 25.4mm × 25.4mm × 34.9mm. Supporting Information Figure S1 shows which blocks in the array had which options available to them. Supporting Information Table S1 contains a list of the magnet block options available to the optimization. The cost function was the % deviation range of B_0 across a 3D grid of uniformly-spaced set of points within the target ROI ($100 \times \Delta B_0/B_0$). We considered a % B_0 range of 5% or less to be useable for the scanner since this would allow a Tx coil with a Q=20 to cover the spin BW. The % B_0 range was computed across the whole volumetric ROI, and not slice-by-slice. Even though we wanted the magnet to have a built-in B_0 gradient for spatial encoding, we did not explicitly target this in the optimization cost function. The design philosophy was that single-sided magnets will naturally have a steep field gradients moving away from the magnet, and a uniform target over the volume would promote both in-plane homogeneity and a reduced G_x gradient.

To constrain the algorithm's ability to trade B_0 field strength for homogeneity, we added a constraint for the minimum allowable B_0. The value of 50mT for this minimum acceptable B0 was chosen based on our previous experience with Halbach permanent magnet assemblies which had a B_0 of 80mT (13,34). Additionally, the starting point for our optimization (a section of a discretized Halbach sphere) was simulated to have B_0=86 mT. Thus we let the algorithm trade off a fraction of this possible B_0 for improved homogeneity.

Prior to optimization, the vector B-field maps for each of the 9 block types were calculated using Comsol (Burlington, MA). Appropriately shifting each block's field map based on the block position and superimposing the fields enabled rapid computation of the magnet assembly's B-field map during optimization. This approach did not account for induced magnetization effects between blocks. We assessed the effect of this field computation approach by simulating a pair of 25.4mm N52-grade magnet cubes spaced 2mm apart using both the superposition-based approach (no block-block interactions) and with Comsol (accounts for block-block interactions). Supporting Information Figure S2 shows the results of this analysis. We found that the superposition approach produced an error of 1mT at 2.7cm from the magnet assembly center, and a 0.1mT error at 6cm away. The shortest distance between a magnet block and the ROI is approximately 6cm, and this error was deemed acceptable. The B_0 field map for the final design was simulated to verify the result. Figure 2d shows the result of the optimization.

B_0 Magnet construction:

The optimal magnet design next was converted into a physically-realizable assembly of NdFeB magnet blocks. The magnet blocks ranged in size from an N45 9.525×25.4×25.4 mm^3 (3/8"x1"x1") block to an N52 25.4×25.4×34.925 mm^3 (1"x1"x1 3/8") block (Figure 3a). Some blocks were constructed by sticking multiple smaller blocks together (eg. an N52 25.4×25.4×28.575 mm^3 (1"x1"x1 1/8") block contained an N52 25.4×25.4×25.4 mm^3 (1"x1"x1") block and an N52 25.4×25.4×3.175 mm^3 (1"x1"x1/8") block). All magnet blocks were purchased online from stock sizes (supplier: Applied Magnets, Plano, TX).

Supporting Information Table S1 details the 9 choices for magnet blocks geometry available to the algorithm. Supporting Information Table S2 describes the manufacturing tolerances. The final assembled blocks were placed into slots in a 3D printed acrylic magnet former (Formlabs model Form 2, Somerville, MA) and were held in place with Loctite 608 epoxy (Figure 3b–c). A 3D field map for the constructed magnet was measured using a 3-axis Hall-effect probe (Metrolab model THM1176, Geneva, Switzerland) positioned by a 3-axis robot. This measured field map was then fit to a 12th-order polynomial. Use of a 12th-order polynomial allowed for spatial interpolation while accurately modeling the unprocessed B_0 map within the ROI. Supporting Information Figure S3 shows the correspondence between the unprocessed and polynomial-fit B_0 maps.

Gradient Coils

Two "cap-shaped" gradient coils were designed for blipped phase encoding of a spin-echo train along the y- and z-axes. These coils were designed on a surface that fit outside the B_0 magnet assembly (Figure 4a). This design choice saved valuable space inside the magnet to enable a stronger B_0 and allowed for improved gradient linearity, at the cost of reduced gradient efficiency. Additionally, in our experience, weak unshielded gradient coils do not produce significant eddy current effects if placed either inside or outside an NdFeB magnet. The gradient winding patterns were designed using a modified Boundary Element Method Stream Function (BEM-SF) solver (37,38) with L2-regularization. Single sided gradients, like single sided magnets have a natural decrease in field amplitude moving away from the structure. For the G_y and G_z gradient, this imparts an additional 2nd-order term (either XY or XZ respectively). In order to facilitate the optimization algorithm in removing these 2nd order terms, we explicitly included negative XY or XZ terms in the optimization cost function. Thus, the target fields included the desired 1st-order terms (Y and Z, respectively) along with one additional 2nd-order term (either XY or XZ, respectively). The amplitude for this second-order cost function term was taken from a design including only a first order cost function. This was found to significantly reduce the variation in gradient efficiency over the target ROI, as shown in Supporting Information Figure S4.

The optimized stream functions were converted into wire winding paths (Figure 4b) which were then projected onto a piecewise-linear surface. This surface was physically constructed by 3D printing (Stratasys Fortus 360mc, Eden Prairie, MN) a polycarbonate helmet former (~2mm thick). A series of triangular and rectangular facets were then epoxied onto the outside of this basic helmet structure. The triangular and rectangular pieces contained grooves for press-fitting two layers of AWG22 magnet wire into the plastic former. After winding the G_y coil, an additional layer of triangular and rectangular grooved pieces was epoxied external to the G_y coil to form the G_z coil. Figure 4 shows the gradient coil wire patterns, constructed gradient coils, as well as the constructed magnet.

The combined magnet and gradient coil fields were mapped using the 3-axis Hall effect probe (Metrolab THM1176). Field measurements were made while each coil was energized with either I=0A or I=2A to provide separate maps of the B_0 and gradient coil fields. These field maps were fit to a 5th-order polynomials subject to the appropriate symmetry constraints about the XY and YZ planes.

RF and imaging console hardware

An RF coil was designed on a surface fitting inside the B_0 magnet using the same BEM stream function approach used for the gradient coils. The same static-field approach used for the gradient design was used because the coil dimension (~0.1m) was much less than the wavelength at the Larmor frequency (f~2.67MHz; lambda~112m). The RF coil winding was designed to optimize spatial B_1 uniformity within the target ROI.

The RF coil was constructed by press-fitting 4 turns of Litz wire (OD=1mm, 195 strands AWG42, New England wire part no. NLC+195/42SNSN, Lisbon, NH) into a 3D-printed polycarbonate former (Stratasys Fortus 360mc) (Figure 5a). A 1-Ohm resistor was placed in series with the coil to increase the 3dB bandwidth to 157kHz (BW without resistor=72kHz). The coil bandwidth was measured by driving the coil with the output port of a network analyzer and measuring the width of the S_{12} response in a pickup coil (field probe). In contrast, the range of Larmor frequencies present in the 3D ROI was ~187 kHz, which is similar to the RF excitation BW (180 kHz for the 2D multislice experiment and 200kHz for the 1D depth profiling). Ideally if the coil Rx bandwidth is determined from losses (which add noise), then the coil Rx bandwidth should be closely matched to the spin BW. Given that Tx efficiency is not a primary issue, the Tx bandwidth should comfortably cover the spin BW. For our case, where a Tx/Rx coil was used, the Tx BW was uncomfortably tight around the spin BW, likely shading some of the ROI.

All experiments used an Apollo console (Tecmag, Houston, Texas, USA) for RF and for gradient waveform generation and signal recording. The RF subsystem used a crossed-diode passive T/R switch, wideband 50-Ohm input preamplifier (MITEQ model AU-1583, Hauppauge, NY), and 2kW-rated 2.5MHz-4.5MHz RFPA (Tomco model BT02000-AlphaS-3MHz, Stepney, SA, Australia). The gradient coils were driven by a pair of home-made current-mode amplifiers built from a push-pull pair of linear op-amps (OPA549, Texas Instruments, Dallas, TX, USA) compensated to provide current controlled output (39). The compensation network was designed for the gradient coil impedance. Each gradient amplifier is capable of driving +−10A with a voltage of +−15V and bandwidth > 20 KHz. The gradient drive was noise-filtered using a 6th-order Butterworth filter (f_c=500kHz). All imaging experiments were performed in a shielded environment (Figure 5b).

Depth profiling experiments

Depth profiling experiments used the built-in B_0 field gradient as a readout encoding gradient. For such experiments, the measured spin-echo spectrum corresponds to a 1D depth profile of the phantom positioned in the sensitive ROI of the magnet as shown in Figure 5b. Depth profiles were acquired using a water bottle phantom (D=63mm) with layered internal structure. The phantom contained three h=5mm layers of aqueous solution (0.2% Gd-DPTA) separated by h=5mm layers of plastic (Figure 5c) and was positioned in the tuned Tx/Rx solenoid at the sensitive ROI of the magnet. Data were acquired using a RARE-type excitation with high-bandwidth frequency-swept pulses (90 and 180 pulse duration=3ms, pulse BW=200kHz, f_c=2.67MHz, peak RF power=32W, TE=10ms, N_{echos}=2, N_{ave}=16, 896 samples acquired with a dwell time of 4us) (40). Both a true 1D acquisition with no y- or z-axis gradient phase encoding and a minimally phase encoded 3D version were obtained. The latter used a 5×5 phase encode acquisition (I_{max}=0.62A and t=1ms gradient moments) giving a 5×5 (14mm × 14mm) set of depth profiles over a FOV_{yz} of ~70mm. Both acquisitions were each repeated with TR=500ms for 64 averages, giving acquisition times of 30sec (1D acquisition) and 11min (3D acquisition). The fixed G_x=117mT/m readout gradient and BW=279[Hz/Px] sampling bandwidth together give a native resolution of 0.056mm, though with low SNR. To address this, the data were retrospectively down-sampled by 16× and filtered to increase SNR, producing a final depth resolution of 0.9mm.

2D multi-slice Imaging experiments

The 2D multi-slice imaging experiments were performed using a cylindrical phantom (diameter = 63mm, height = 40mm) with different internal structure at different heights (Figure 5d), and filled with Gd-DPTA (0.05%) solution. Images were acquired at 6 slice positions in the phantom using a slice-interleaved RARE sequence with 31 × 31 phase-encode matrix. The sequence phase encodes in y along the N_{echos}=32 echo train (the first echo is discarded) and then loops through the second phase encode direction (z) with a TR = 1.0s. The phase encode blips (trapezoid blip duration = 1ms, using I_{max} = 4.62A) were set to provide an YZ-plane resolution of ~2×2mm. We used echo-spacing = 3ms; BW = 1736[Hz/Px]; and N_{ave} = 24. The total acquisition time including dummy shots was 12m 40s.

All RF pulses in the sequence were Tukey-windowed sinc pulses (BW=30kHz; t_p=110ms) centered at 6 equally spaced frequencies from 2.60MHz to 2.75MHz (peak Tx power = 315W). These pulses excite slices whose shapes are defined by the built-in isochromats of the inhomogeneous B_0 magnet (41), with this pulse bandwidth providing a slice thickness of 6mm for the ROI center where the gradient strength is 117mT/m. The expected slice thickness at the edges of the ROI (distal and proximal to the RF coil) are 4mm and 8mm.

Images were reconstructed using the average of the center three points of each spin echo, and by doing Fourier reconstruction along the y- and z- phase encode directions. Exponential-window apodization was performed along the shot-shot phase encode dimension.

Results

B_0 Magnet

Figure 6 shows simulated and measured field maps for the B_0 magnet. Supporting Information Figure S5 shows the same field maps with the same color scale. The simulated field map had a mean B_0 of 68.5mT within the ROI, while the constructed magnet had a mean B_0 of 63.6mT. The B_0 ranges across the ROI were 4.77mT (simulated) and 4.40mT (measured). The constructed magnet had a built-in field gradient of ~117mT/m (~5000Hz/mm). The magnet (including former) weighed 6.3kg and contained magnet material costing under $450 (USD).

Gradient coils

Figure 7 shows B_z field maps for the gradient coils at I=1A. The G_y coil had an efficiency of 1.117 mT/m/A at the ROI center and linearity of 33.3% (along the y-axis); the G_z coil had a mean efficiency of 1.019 mT/m/A at the ROI center and a linearity of 27.8% (along the z-axis). Across the ROI, G_y coil efficiency ranged from 0.979 mT/m/A to 1.348 mT/m/A; G_z coil efficiency ranged from 0.845 mT/m/A to 1.03 mT/m/A. The inductances of coils were: 273.3 uH (G_y) and 178 uH (G_z). The G_y and G_z coil DC resistances were 1.15 Ω and 1.01 Ω respectively.

1D depth profiling

Figure 8 plots the signal versus readout frequency for the 1D and 3D-encoded depth profiling acquisitions. In all plots, three peaks corresponding to the three compartments of the phantom can be visually identified. The spectra obtained from the 3D acquisition show more-pronounced spacing between these peaks. The shape of the phantom appears weighted by a Gaussian-shaped envelope, corresponding to the limited RF coil and pulse bandwidth. This projection has a depth resolution between 0.7mm and 1.1mm based on the known gradient variation across the object and sampling rate.

2D Multislice imaging

Figure 9 shows the 6 imaging slices from the multislice acquisition. The top-left slice (f_c=2.60 MHz) corresponds to a slice located in the uniform region of the phantom. The bottom-right slice (f_c = 2.75 MHz) mostly corresponds to a signal-free region below the bottom of the phantom. In several slices, the phantom appears truncated in the z-dimension. This truncation boundary corresponds to a highly-inhomogeneous region of the B_0 map. This results in a reduction in sensitive ROI size along the z-dimension.

Discussion

The system demonstrated the ability of a point-of-care system to acquire 1D and 3D images over a reduced FOV sensitive region. As desired, the system is lightweight (under 10kg) and can be attached to a posable arm. The cost of system components is low (magnet material under $450 USD and gradient driver parts cost ~$100 USD per channel.) In short, the prototype MR Cap satisfies our design objective to create a 3D brain imaging device that is lightweight, portable, and low-cost. However, several limitations exist in the presented system.

Depth Profiling

The measured depth profiles in Figure 7 do not precisely match the structure of the phantom. This is especially apparent for the depth profile measured without YZ-plane phase encoding - in this measurement, three peaks are visible, but they overlap and their boundaries are blurred. This is likely a consequence of the misalignment between the imaging phantom structure and the isochromats of the B_0/readout encoding field whereby phantom structures are spread out over a large number of readout frequencies. This is in contrast to traditional NMR depth profiling with highly-planar isochromats matching a sample with planar, laminar structure. Precise alignment of the magnetic field and sample enables the acquisition of high-resolution depth profiles (42). This approach has been used to measure artwork composition (43,44), to assess surface degradation of materials (21), and for biomedical applications (42) such as skin profiling (26). Successful extension to depth profiles 1–2cm into the human brain could potentially to assess pathologies of the dura and detect subdural hematomas. However, the acquisition of high-resolution *in vivo* cerebral depth profiles will be challenging given human anatomical variation and the difficulty of aligning the anatomy of interest with the magnetic field isochromats. In this work, we found that a 3D acquisition with low-resolution in-plane phase encoding produced higher-quality depth profiles of a phantom than a true 1D depth acquisition. This suggests that such an approach may also help *in vivo*.

Image Artifacts

The z-dimension of the sensitive ROI was truncated by approximately 4cm less than the design target in several imaging slices (Figure 10a). This likely results from the highly-inhomogeneous B_0 field in that region – i.e. the static gradient in that location is steeper. One effect of this is a reduction in slice thickness and an associated reduction in signal level. Additional issues that may arise are T_2 signal losses due to diffusion effects and a shortening of the local T_2*. T_2* decay is largely refocused at the center of each spin echo, but we averaged together the center three points of each spin echo during image reconstruction, introducing a dependence on local T_2*. Mitigation of this effect (restoration of this lost FOV) would require either the application of shimming capability to the existing magnet or a new design where the optimization more explicitly penalized peak (“min-max”) inhomogeneities. Furthermore, until more experience is gained with such systems, the clinical implication of the reduced FOV is not clear. In fact, reducing the FOV is sometimes desired in MRI to focus on an anatomical region of interest or to reduce the image encoding burden required to avoid aliasing (45,46). The MR Cap, by design, is such a “zoomed” acquisition device.

Figure 10b shows another image artifact: hyperintense regions in the $f_c = 2.72$ MHz slice of the 3D acquisition. These likely result from the non-uniform slice thickness arising from the B_0 field and the fixed BW RF pulses. The RF pulses were designed to have uniform frequency content in a 30 kHz bandwidth (in this case, between 2.705 MHz and 2.735 MHz). However, given the curving shape and changing gradient within the B_0 map, the excited slice varies in thickness throughout the imaging volume (Figure 10b). The flattened region of B_0 variation results in the two peaks in the slice thickness at the edge of the z FOV, as shown in the computed plot of slice thickness as a function of z location (Figure 10b). This artifact could be superficially addressed with an image normalization procedure.

Because of the G_y gradient strength non-linearity, the $f_c = 2.72$ MHz and $f_c = 2.60$ MHz slices were observed to have different fields-of-view along the y-axis (FOV_y). The phantom (D=63mm) extended 31 pixels and 25 pixels in the two slices, corresponding to an FOV_y of 63mm ($f_c = 2.72$ MHz slice) and 78mm ($f_c = 2.60$ MHz slice) (Figure 10c). Using the measured G_y coil field at z=0 in these two slices in combination with the known acquisition parameters, the expected FOV_ys are 59mm ($f_c = 2.72$ MHz slice) and 75mm ($f_c = 2.60$ MHz slice). These are 6.3% and 3.9% lower than the respective image-derived FOV_ys, but explain the observed trend. These gradient non-linearity effects could be mitigated by refining the coil design or compensated for in the sequence by adjusting the encoded FOV for each slice.

Other options include post-processing approaches which apply a gradient nonlinearity correction (47,48) or generalized image reconstruction (49) approach.

The image SNR in Figure 10 varies from slice to slice. There are likely three reasons for this: (1) a progressive reduction in slice thickness resulting from the steeper B_0 gradient (i.e., slice-select gradient) at deeper locations; (2) the RF coil provides progressively reduced Rx and Tx capabilities for pixels regions more distant from the RF coil/magnet assembly; and (3) the resonance frequency for the deeper slices begin to exceed the RF coil bandwidth.

As described above, control of the built-in B_0 gradient is critical to providing equal amounts of signal per unit bandwidth at different positions in the ROI. An improved magnet design with higher linearity (but limited gradient stength) would mitigate artifacts. Additionally an RF coil with increased spatial uniformity and coverage would improve images. This would likely involve either a physically larger RF coil or an RF coil with more windings. Adding windings of increasing size boosts the inductance of the coil more quickly than the resistance. Unfortunately, this in turn would increase the Q of the coil and decrease its bandwidth, exacerbating the coil BW issue. Resolving issues stemming from narrow coil bandwidth can be approached by shaping the spectral resonance response of the coil. Several approaches have been proposed for effectively creating a coil with a more uniform frequency response than the typical simple LC circuit without using a series resistor, as we did. These include quasi-transmission line coils (50), coupled resonant structures (51), use of a low-impedance preamplifier (52), and inductively coupled negative feedback mechanisms (53). However, it must be verified that any employed Q-broadening technique not only creates a wide-bandwidth receive chain, but actually does so in a loss-less way and thus improves the SNR across that bandwidth.

While spatially non-uniform sensitivity can be problematic, it is routinely encountered and managed in modern high-field MRI scanners using multi-channel Rx arrays (54). Practitioners have come to appreciate that it is more important to achieve acceptable image SNR over the desired field of view. In summary, this could be done either with improved system hardware or with more general image reconstruction or post-processing schemes.

SNR

The MR-Cap, like other low field MR approaches, has intrinsic SNR limitations. A stronger B_0 magnet in the same form factor is likely achievable by allowing for a higher density of magnetic material or perhaps by adding a second layer or otherwise increasing the cap thickness. A more uniform magnet could likely be realized by more thoroughly exploring the parameter space of possible magnet designs or the use of B_0 shim coils or shim material.

An improved RF coil would also increase SNR. Adding the 1-Ohm resistor increased the coil 3dB BW from 72kHz to 157kHz, corresponding to an increase in the series resistance of the coil from 0.85 Ohm to 1.85 Ohm. This causes a 48% increase in noise standard deviation and thus a 32% drop in SNR. Removing this resistor and increasing the BW with more sophisticated, lossless approaches would improve performance. This coil has intrinsic resistance of 0.85 Ohm (measured from the unloaded Q) and a measured inductance of 3.5 uH. Theoretically, the Fano theory of matching networks suggests that a lossless matching network could achieve a flat, −5.9dB match across 180kHz BW for this coil (55). It is not clear how to obtain this in practice and the noise figure of the practical network would need to be assessed.

Acquisition improvements could also increase image SNR. Weighting the sampling density to the center of k-space or utilizing sparsity priors such as compressed-sensing type acquisitions or denoising approaches have been used to boost SNR in other low-field systems (56). A flipback pulse after each RARE train may assist with longitudinal M_z recovery and increase available signal (57). The spin echoes in the 3D acquisition are temporally very narrow (due to field inhomogeneity), and the acquisition window length could be significantly shortened. This would free up sequence time for more echoes, allowing averaging down the echo train. Such an approach may be impractical at high field due to safety limits on the RF specific absorption rate (SAR), but at 64mT the SAR for such an acquisition is negligible.

Diffusion Effects

The MR Cap B_0 field contains a large built-in G_x gradient (G_x=117 mT/m), which leads to diffusion-induced signal attenuation for the first echo the RARE characterized by the b value: $b_{first} = \frac{\gamma^2 G^2 D(TE)^3}{12}$. For the first echo of the multislice sequence (TE=3ms), b_{first} = 2.2 s/mm^2 for the TE = 3ms used resulting in a negligible (~0.5%) signal loss to diffusion for the center of k-space for this sequence. For the nth echo of a RARE sequence, b = b_{first}*n (58) and larger diffusion weightings can be obtained by either increasing the echospacing or re-ordering kspace to sample k=0 at a later echo. Thus, using a RARE readout train allows one to vary diffusion weighting independently of TE (58), and has been explored as a way to obtain diffusion-weighted images in inhomogeneous fields (59).

Practical Considerations

There are several practical requirements to overcome before the MR Cap could be deployed for point-of-care clinical care. First, the multislice phantom images were acquired in a shielded box and thus did not demonstrate *in vivo* imaging in unshielded environment. Practical point-of-care use would require either a passive shielding approach such as draped conductive cloth, or an active interference cancellation system (60,61). Permanent magnet systems are notorious for temperature induced drift in B_0. While this was not controlled here, standard approaches include either a feedback system controlling a heater to stabilize the temperature, use of a combination of rare-earth materials with differing temperature coefficients (62), or the use of a field probe to measure B_0 drift for incorporation into a model-based image reconstruction algorithm (13). Finally, performance of the MR Cap for scanning a head-sized object that is larger than the target FOV must be assessed.

Additionally, while the MR Cap itself, T/R switch, GPAs, and preamplifier are all highly compact and cost effective, several high-cost, laboratory grade instruments were used. For example, the RF power amplifier (cost ~$15000 USD) and console (~$35000 USD) used in these experiments were not optimized for cost or portability. The 2 kW RF amplifier used was larger than needed and could also likely be reduced in size by using a narrow-band and lower power design. For example, it could potentially be replaced by a previously published low-cost LDMOS amplifier capable of achieving 1.4kW at a cost of $1500 USD (63). Likewise, there has been recent effort towards compact, low-cost MRI consoles (64–68) that could be a great cost-savings, such as the $500 FPGA based open-source system (65). A total bill of materials cost using these two low-cost options is provided in Supporting Information Table S3, detailing a potential total system parts cost of $3350 USD.

The MR Cap was designed to be highly portable and lightweight capable of use with minimal patient movement or transport. Realizing such a light-weight device required a reduced imaging FoV and a highly-inhomogeneous main magnetic field. In contrast, a head-sized cylindrical magnet could achieve a larger imaging FoV and greater field homogeneity, and would potentially have greater imaging capabilities. However, our previous work (13,34) suggests that this approach results in a heavier magnet (roughly 10×). Additionally, like conventional systems, it would require moving the patient's head into the bore. We do not attempt to break this trade-off, but simply demonstrate a system at the extreme edge of this spectrum. Ultimately, if the full spectrum of scanner tradeoffs is available, each usage setting and clinical application will decide the appropriate scanner for the job.

Potential Applications

Possible clinical applications for the MR Cap include point-of-care assessment of cerebral hemorrhage such as subdural hematomas in trauma (69) or post-surgery (70). In the latter, we envision potentially using the device as a monitoring instrument during post-surgical recovery in a neuro-ICU to provide early warning of hemorrhage. Also it would be nice if a PoC system could rule out hemorrhage in potential stroke, allowing earlier rTPA administration (i.e. by EMT prior to transport to a hospital). This latter application will require a clinical trial to make sure we can see hemorrhages, especially deep pathology without T2* contrast (which is difficult at low field.) Other areas where a PoC MR device might be useful is in the neonatal ICU, where transport out of the facility is undesired. While small-footprint scanners that can be sited in the neonatal ICU are on the market, it might be beneficial to have a device that can provide diagnostic information such cerebral hemorrhage assessment without removing the neonate from the isolette.

In addition to extending MRI applications to PoC sites, significantly reducing the equipment and siting costs of an MRI scanner might extend the impact of MRI diagnostic techniques, even if the scanner had a narrow clinical focus. As discussed in the Introduction, there is precedent for this in other imaging modalities, and there are large sections of the Global South and Global North with relatively sparse access to MRI (6).

From a physics point of view, many of these clinical applications would require further refinement, including a PoC usable, flexible, conductive fabric shielding or active RF interference cancellation systems. Sequence requirements include the ability to obtain T2, FLAIR T2, proton density and possibly diffusion contrast, all of which are accessible to a RARE sequence. Certain types of sequences are not well suited to the built-in gradient of the system, including most of the gradient-echo class of sequences (further handicapping T2* imaging). These "RARE sequence accessible" contrasts can also, of course, be obtained with reduced image encoding, such as depth profile imaging. Here, reduced image information is traded for PoC simplicity and speed to answer a simple “yes/no” clinical question in the field, such as: “does the accident victim have a bleed?”

Finally, the built-in B_0 gradient field of 117mT/m is larger than the gradient amplitudes achievable on existing clinical scanners. Nonetheless, the RARE echo train can be arranged to reduce diffusion weighting, and the porous media community has developed pulse sequences to probe diffusion contrast even in the presence of strong static field gradients by modulating the RARE acquisition (71). This method was recently evaluated for applicability to in vivo brain imaging (59).

Conclusion

We demonstrate the MR Cap, a light-weight MRI device for brain imaging with a reduced FOV. The system is low cost (magnet material cost <$450 USD) and lightweight (<10kg), potentially having utility as a point-of-care MRI device in many clinical applications. As an initial step in this direction, we constructed a working prototype system and validated its imaging capabilities in 1D and 3D images over a ~3×8×8 cm^3 volume.

Supplementary Material

Refer to Web version on PubMed Central for supplementary material.

Acknowledgements

We would like to acknowledge: Thomas Witzel for the GPA design, and Matthew Rosen for console assistance and helpful discussions. Research reported in this publication was supported by the National Institute of Biomedical Imaging and Bioengineering of the National Institutes of Health under award numbers: NIH R01EB018976, NIH R00EB021349, and NIH 5T32EB1680.

References

1. Nelson BP, Chason K. Use of ultrasound by emergency medical services: a review. Int. J. Emerg. Med 2008;1:253–259. doi: 10.1007/s12245-008-0075-6. [PubMed: 19384639]
2. Becker L, Kruger GH, Tafoya MJ. The use of portable ultrasound devices in low- and middle-income countries: a systematic review of the literature. Trop. Med. Int. Heal 2016;21:294–311. doi: 10.1111/tmi.12657.
3. Baran JM, Webster JG. Design of Low-Cost Portable Ultrasound Systems: Review In: 2009 Annual International Conference of the IEEE Engineering in Medicine and Biology Society IEEE; 2009 pp. 792–795. doi: 10.1109/IEMBS.2009.5332754.
4. Rumboldt Z, Huda W, All JW. Review of Portable CT with Assessment of a Dedicated Head CT Scanner. Am. J. Neuroradiol 2009;30:1630–1636. doi: 10.3174/ajnr.A1603. [PubMed: 19661166]
5. Heller S, Zanzonico P. Nuclear Probes and Intraoperative Gamma Cameras. Semin. Nucl. Med. [Internet] 2011;41:166–181. doi: 10.1053/j.semnuclmed.2010.12.004.
6. Geethanath S, Vaughan JT. Accessible Magnetic Resonance Imaging: J. Magn. Reson. Imaging 2019:1–13. doi: 10.1002/jmri.26638.
7. Marques JP, Simonis FFJ, Webb AG. Low-Field MRI: An MR Physics Perspective 2019:1–15. doi: 10.1002/jmri.26637.
8. Lother S, Schiff SJ, Neuberger T, Jakob PM, Fidler F. Design of a mobile, homogeneous, and efficient electromagnet with a large field of view for neonatal low − field MRI. Magn. Reson. Mater. Physics, Biol. Med 2016;29:691–698. doi: 10.1007/s10334-016-0525-8.

9. Kraus RJ, Espy M, Magnelind P, Volegov P. Ultra-low field nuclear magnetic resonace Oxford University Press; 2014.
10. Sarracanie M, Lapierre CD, Salameh N, Waddington DEJ, Witzel T, Rosen MS. Low-Cost High-Performance MRI. Sci. Rep. [Internet] 2015;5:15177. doi: 10.1038/srep15177.
11. Macovski A, Conolly S. Novel Approaches to Low-Cost MRI 1993:221–230.
12. Obungoloch J, Harper JR, Consevage S, Savukov IM, Neuberger T, Tadigadapa S, Schiff SJ. Design of a sustainable prepolarizing magnetic resonance imaging system for infant hydrocephalus. Magn. Reson. Mater. Physics, Biol. Med. [Internet] 2018;31:665–676. doi: 10.1007/s10334-018-0683-y.
13. Cooley CZ, Stockmann JP, Armstrong BD, Sarracanie M, Lev MH, Rosen MS, Wald LL. Two-dimensional imaging in a lightweight portable MRI scanner without gradient coils. Magn. Reson. Med. [Internet] 2015;73:872–83. doi: 10.1002/mrm.25147.
14. Zimmerman RA, Bilaniuk LT, Goldberg HI, Grossman RI, Levine RS, Lynch R, Edelstein W, Bottomley P, Redington R. Cerebral NMR Imaging: Early Results with a 0.12 T Resistive System. Am. J. Roentgenol 1983;141:1187–1193. [PubMed: 6606315]
15. Blanco RT, Ojala R, Kariniemi J, Per J, Niinim J, Tervonen O. Interventional and intraoperative MRI at low field scanner – a review. Eur. J. Radiol 2005;56:130–142. doi: 10.1016/j.ejrad.2005.03.033. [PubMed: 15908156]
16. Vaughan JT, Wang B, Idiyatullin D, Sohn S, Jang A, BelaBarra L, Garwood M. Progress Toward a Portable MRI System for Human Brain Imaging In: ISMRM; 2016 p. 498.
17. Gold G, Theodorou D, Blair T, Garcia G, Crowley C, Rose F, Trudell D, Resnick D. MR Imaging of the Wrist with a Portable Extremity Scanner 1994;182:92122.
18. Lindegaard HM, Vallo J, Horslev-Petersen K, Junker P, Ostergaard M. Low-cost, low-field dedicated extremity magnetic resonance imaging in early rheumatoid arthritis: a 1-year follow-up study. Ann Rheum Dis 2006;65:1208–1212. doi: 10.1136/ard.2005.049213. [PubMed: 16540550]
19. Crues JV, Shellock FG, Dardashti S, James TW, Troum OM. Identification of Wrist and Metacarpophalangeal Joint Erosions Using a Portable Magnetic Resonance Imaging System Compared to Conventional Radiographs. J. Rheumatol 2004;31:676–685. [PubMed: 15088291]
20. Casanova F, Perlo J, Blümich B. Single-Sided NMR 1st ed. Berlin Heidelberg: Springer-Verlag; 2011.
21. Goga NO, Demco DE, Kolz J, Ferencz R, Haber A, Casanova F, Blümich B. Surface UV aging of elastomers investigated with microscopic resolution by single-sided NMR. J. Magn. Reson 2008;192:1–7. doi: 10.1016/j.jmr.2007.10.017. [PubMed: 18294890]
22. Judeinstein P, Ferdeghini F, Oliveira-silva R, Zanotti J, Sakellariou D. Low-field single-sided NMR for one-shot 1D-mapping: Application to membranes. J. Magn. Reson. [Internet] 2017;277:25–29. doi: 10.1016/j.jmr.2017.02.003.
23. Jackson JA. Remote NMR well logging. Geophysics 1981;46:415.
24. Xu Z, Morris RH, Bencsik M, Newton MI. Detection of virgin olive oil adulteration using low field unilateral NMR. Sensors (Switzerland) 2014;14:2028–2035. doi: 10.3390/s140202028.
25. Eidmann G, Savelsberg R, Blümler P, Blümich B. The NMR MOUSE, a mobile universal surface explorer. J. Magn. Reson. - Ser. A 1996;122:104–109. doi: 10.1006/jmra.1996.0185.
26. Van Landeghem M, Danieli E, Perlo J, Blümich B, Casanova F. Low-gradient single-sided NMR sensor for one-shot profiling of human skin. J. Magn. Reson. [Internet] 2012;215:74–84. doi: 10.1016/j.jmr.2011.12.010.
27. Tourell MC, Ali TS, Hugo HJ, Pyke C, Yang S, Lloyd T, Thompson EW, Momot KI. Magnetic Resonance in Medicine T 1 -based sensing of mammographic density using single-sided portable NMR 2018:1–9. doi: 10.1002/mrm.27098.
28. Li M, Vassiliou CC, Colucci L a, Cima MJ. (1)H nuclear magnetic resonance (NMR) as a tool to measure dehydration in mice. NMR Biomed. [Internet] 2015;28:1031–9. doi: 10.1002/nbm.3334.
29. Bashyam A, Li M, Cima MJ. Design and experimental validation of Unilateral Linear Halbach magnet arrays for single-sided magnetic resonance. J. Magn. Reson. [Internet] 2018;292:36–43. doi: 10.1016/j.jmr.2018.05.004.
30. Perlo J, Casanova F, Blümich B. 3D imaging with a single-sided sensor: An open tomograph. J. Magn. Reson 2004;166:228–235. doi: 10.1016/j.jmr.2003.10.018. [PubMed: 14729034]

31. McDaniel PC, Cooley CZ, Stockmann JP, Wald LL. A 6.3kg Single-Sided Magnet for 3D, Point-of-Care Brain Imaging In: Proc Intl Soc Mag Reson Med, Paris, France; 2018 p. 943.
32. Cooley CZ, Haskell MW, Cauley SF, Sappo C, Lapierre CD, Ha CG, Stockmann JP, Wald L. Design of sparse Halbach magnet arrays for portable MRI using a genetic algorithm 2015:1–14.
33. Leupold H, Potenziani E II. Novel High-Field Permanent-Magnet Flux Sources. IEEE Trans. Magn 1987;MAG-23:3628–3629.
34. Cooley CZ, Haskell MW, Cauley SF, Sappo C, Lapierre CD, Ha CG, Stockmann JP, Wald LL. Design of Sparse Halbach Magnet Arrays for Portable MRI Using a Genetic Algorithm. IEEE Trans. Magn 2017.
35. Raich H, Blümler P. Design and construction of a dipolar Halbach array with a homogeneous field from identical bar magnets: NMR mandhalas. Concepts Magn. Reson. Part B Magn. Reson. Eng 2004;23:16–25. doi: 10.1002/cmr.b.20018.
36. Turek K, Liszkowski P. Magnetic field homogeneity perturbations in finite Halbach dipole magnets. J. Magn. Reson. [Internet] 2014;238:52–62. doi: 10.1016/j.jmr.2013.10.026.
37. Peeren GN. Stream function approach for determining optimal surface currents. J. Comput. Phys 2003;191:305–321. doi: 10.1016/S0021-9991(03)00320-6.
38. Bringout G, Gräfe K, Buzug TM. Performance of Shielded Electromagnet-Evaluation Under Low-Frequency Excitation. Ieee Trans. Magn 2015;51:1–4. doi: 10.1109/TMAG.2014.2329396. [PubMed: 26203196]
39. Cooley CZ, Stockmann JP, Lapierre C, Witzel T, Jia F, Zaitsev M, Stang P, Scott G, Wenhui Y, Zheng W. Implementation of low-cost, instructional tabletop MRI scanners. Proc. ISMRM 2014;22:4819.
40. Casabianca LB, Mohr D, Mandal S, Song Y, Frydman L. Chirped CPMG for well-logging NMR applications. J. Magn. Reson. [Internet] 2014;242:197–202. doi: 10.1016/j.jmr.2014.02.025.
41. Sarty GE, Vidarsson L. Magnetic resonance imaging with RF encoding on curved natural slices. Magn. Reson. Imaging [Internet] 2018;46:47–55. doi: 10.1016/j.mri.2017.10.007.
42. Danieli E, Blümich B. Single-sided magnetic resonance profiling in biological and materials science. J. Magn. Reson. [Internet] 2013;229:142–154. doi: 10.1016/j.jmr.2012.11.023.
43. Presciutti F, Perlo J, Casanova F, et al. Noninvasive nuclear magnetic resonance profiling of painting layers Noninvasive nuclear magnetic resonance profiling of painting layers 2008;33505:1–4. doi: 10.1063/1.2963026.
44. Blümich B, Haber A, Casanova F, Del Federico E, Boardman V, Wahl G, Stilliano A, Isolani L. Noninvasive depth profiling of walls by portable nuclear magnetic resonance 2010:3117–3125. doi: 10.1007/s00216-010-3880-8.
45. Feinberg DA, Hoenninger JC, Crooks LE, Kaufman L, Watts JC, Arakawa M. Volume MR Imaging: and Their. Radiology 1985;156:743–747. [PubMed: 4023236]
46. Luo Y, De Graaf RA, Delabarre L, Tannu A, Garwood M. BISTRO: An Outer-Volume Suppression Method That Tolerates RF Field Inhomogeneity. Magn. Reson. Med 2001;45:1095–1102. [PubMed: 11378888]
47. Sumanaweera T, Glover G, Song S, Adler J, Nape S. Quantifying MRI Geometric Distortion in Tissue. Magn. Reson. Med 1994;31:40–47. [PubMed: 8121267]
48. Langlois S, Desvignes M, Constans J, Revenu M. MRI Geometric Distortion: A Simple Approach to Correcting the Effects of Non-Linear Gradient Fields. J. Magn. Reson 1999;9:821–831.
49. Lin F, Witzel T, Schultz G, Gallichan D, Kuo W, Wang F, Hennig J, Zaitsev M, Belliveau JW. Reconstruction of MRI Data Encoded by Multiple Nonbijective Curvilinear Magnetic Fields. Magn. Reson. Med. Sci 2012;68:1145–1156. doi: 10.1002/mrm.24115.
50. Scharfetter H, Petrovic A, Eggenhofer H, Stollberger R. A no-tune no-match wideband probe for nuclear quadrupole resonance spectroscopy in the VHF range. Meas. Sci. Technol. [Internet] 2014;25:125501. doi: 10.1088/0957-0233/25/12/125501.
51. Raad A, Darrasse L. Optimization of NMR receiver bandwidth by inductive coupling. Magn. Reson. Imaging 1992;10:55–65. doi: 10.1016/0730-725X(92)90373-8. [PubMed: 1545682]
52. Roemer PB, Edelstein WA, Hayes CE, Souza SP, Mueller OM. The NMR phased array. Magn. Reson. Med 1990;16:192–225. [PubMed: 2266841]

53. Mandal S, Utsuzawa S, Cory DG, Hürlimann M, Poitzsch M, Song YQ. An ultra-broadband low-frequency magnetic resonance system. J. Magn. Reson. [Internet] 2014;242:113–125. doi: 10.1016/j.jmr.2014.02.019.
54. Hayes CE, Hattes N, Roemer PB. Volume Imaging with MR Phased Arrays. Magn. Reson. Med 1991;18:309–319. [PubMed: 2046514]
55. Fano RM. Theoretical limitations on the broadband of arbitrary impedances 1948.
56. Sarracanie M, Armstrong BD, Stockmann J, Rosen MS. High Speed 3D Overhauser-Enhanced MRI Using Combined b-SSFP and Compressed Sensing 2014;745:735–745. doi: 10.1002/mrm.24705.
57. Becker ED, Ferretti JA, Farrar TC. Driven Equilibrium Fourier Transform Spectroscopy: A New Method for Nuclear Magnetic Resonance Signal Enhancement. J. Am. Chem. Soc 1969;380:7784–7785. doi: 10.1021/ja50001a068.
58. Carr HY, Purcell EM. Effects of Diffusion on Free Precession in Nuclear Magnetic Resonance Experiments. Phys. Rev 1954;94:630–638.
59. Stockmann JP, McDaniel PC, Vuahgn C, Cooley CZ, Wald LL. Feasibility of brain pathology assessment with diffusion imaging on a portable scanner using a fixed encoding field Frequency-swept RF pulses are used to excite and refocus spins across the wide bandwidth of the inhomogeneous B 0 field (~ 100 KHz) [7] In: ISMRM; 2019 p. 1196.
60. Walsh DO. Noise canceling in-situ NMR detection 2011:US 20110109311A1.
61. Rearick R, Charvat GL, Rosen MS, Rothberg JM. Noise suppression methods and apparatus 2017:US009625543B2.
62. Danieli E, Perlo J, Blümich B, Casanova F. Highly Stable and Finely Tuned Magnetic Fields Generated by Permanent Magnet Assemblies. Phys. Rev. Lett 2013;110:180801. doi: 10.1103/PhysRevLett.110.180801. [PubMed: 23683185]
63. Bluecher C, Han H, Hoffmann W, Seemann R, Seifert F, Niendorf T, Winter L. COSI Transmit: Open Source Soft- and Hardware Transmission System for traditional and rotating MR In: ISMRM; 2017 p. 1055.
64. Hasselwander CJ, Cao Z, Grissom WA. gr-MRI: A software package for magnetic resonance imaging using software defined radios. J. Magn. Reson. [Internet] 2016;270:47–55. doi: 10.1016/j.jmr.2016.06.023.
65. Anand S, Stockmann JP, Wald LL, Witzel T. A low-cost (<$500 USD) FPGA-based console capable of real-time control In: Proc Intl Soc Mag Reson Med, Paris, France; 2018 p. 948.
66. Webber JBW, Demin P. Credit-card sized fi eld and benchtop NMR relaxometers using fi eld programmable gate arrays. Magn. Reson. Imaging [Internet] 2019;56:45–51. doi: 10.1016/j.mri.2018.09.018.
67. Khandagle K Implementation of MRI Gradient Generation System and Controller on Field Programmable Gate Array (FPGA). 2018 Int. Conf. Commun. Inf. Comput. Technol 2018:1–4. doi: 10.1109/ICCICT.2018.8325876.
68. Chen H, Kim Y, Nath P, Hilty C. An ultra-low cost NMR device with arbitrary pulse programming. J. Magn. Reson. [Internet] 2015;255:100–105. doi: 10.1016/j.jmr.2015.02.011.
69. Lee B, Newberg A. Neuroimaging in Traumatic Brain Imaging 2005;2:372–383.
70. Zacko C, LeRoux P. Perioperative neurosurgical critical care In: Neurocritical Care Society Practice Update, Philadelphia, PA; 2013.
71. Hurlimann MD. Diffusion and Relaxation Effects in General Stray Field NMR Experiments. J. Magn. Reson 2001;378:367–378. doi: 10.1006/jmre.2000.2263.

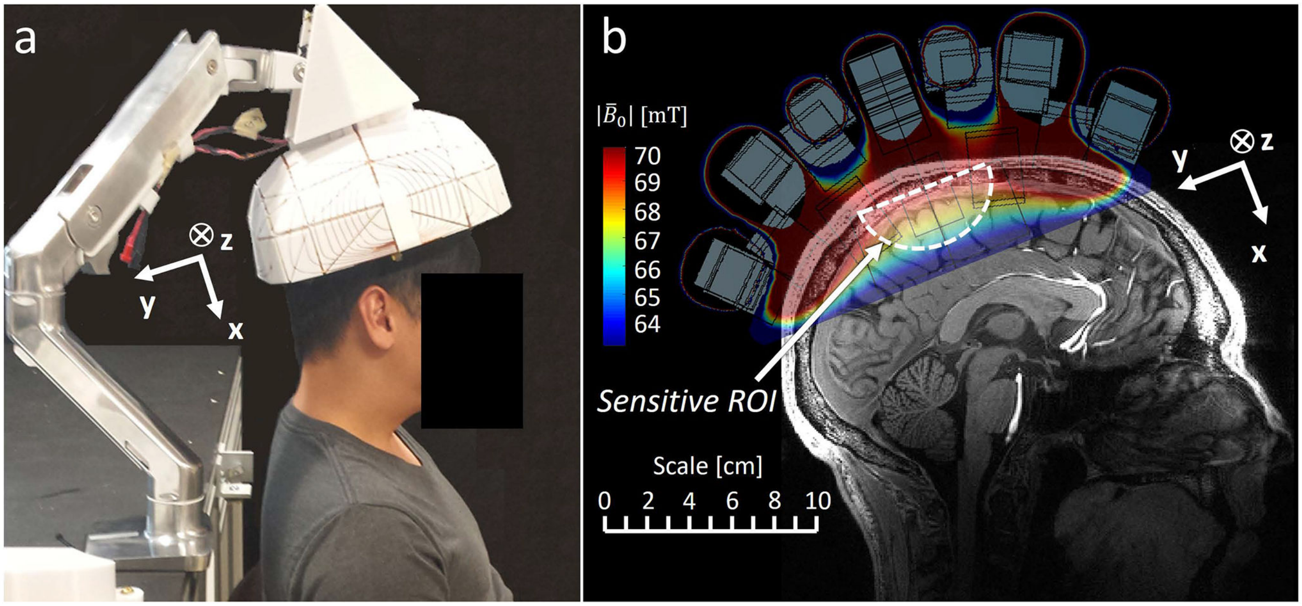
[redacted]

Figure 1:

(a) Concept drawing of the “MR Cap” illustrating how the system might be positioned and moved about the subject’s head. (b) Concept drawing illustrating a proposed B_0 map with built-in readout encoding gradient. The design ROI is imposed on a high-field anatomical MR image.

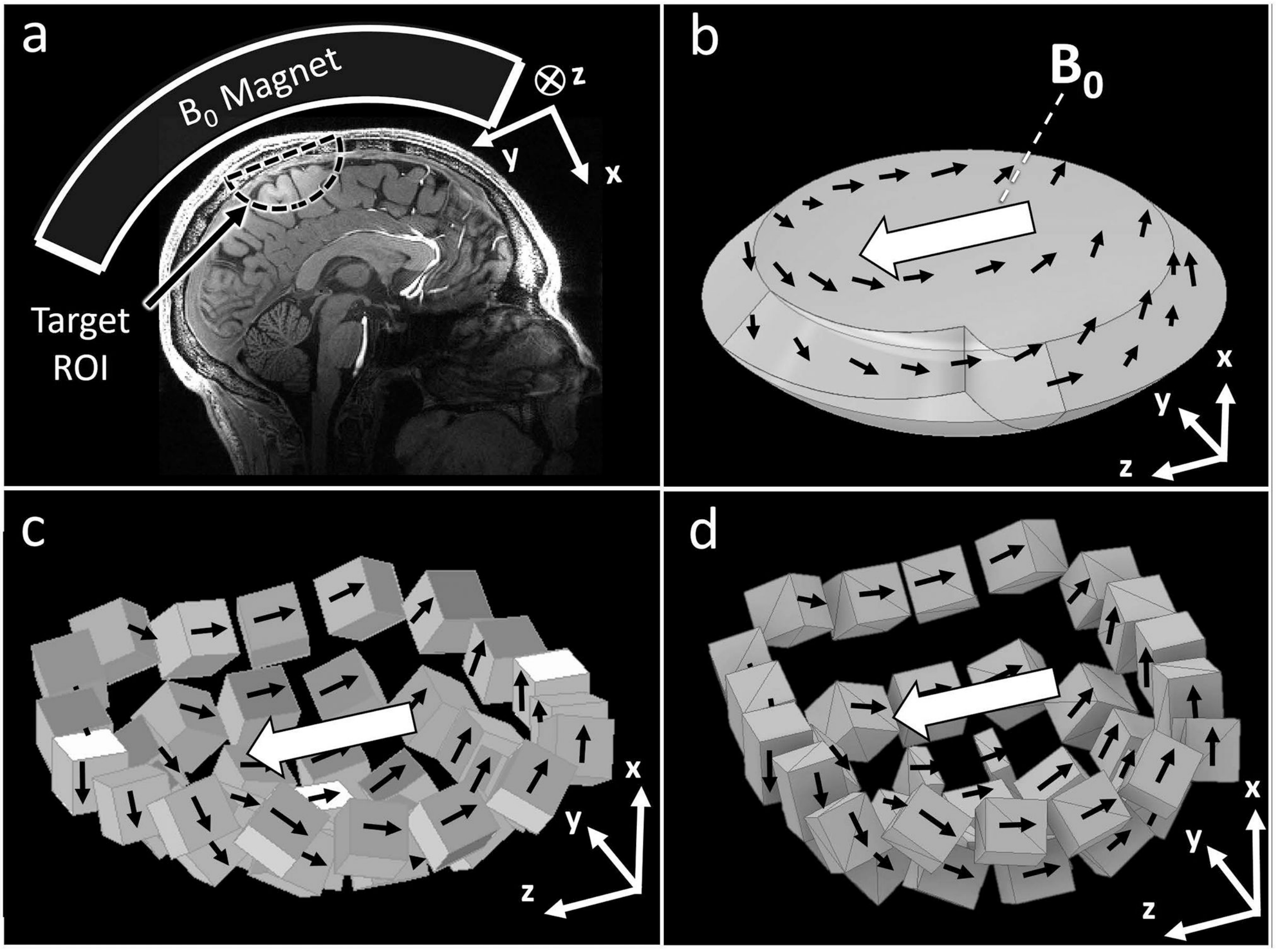

Figure 2:

(a) Illustration showing approximate desired magnet shape, ROI, and B_0 axis. (b) Section of Halbach sphere magnet that approximates the desired magnet shape and B_0 direction. (c) Discretized Halbach sphere section that approximates the continuous magnet design as an assembly of magnet blocks. (d) Optimized discrete block magnet design

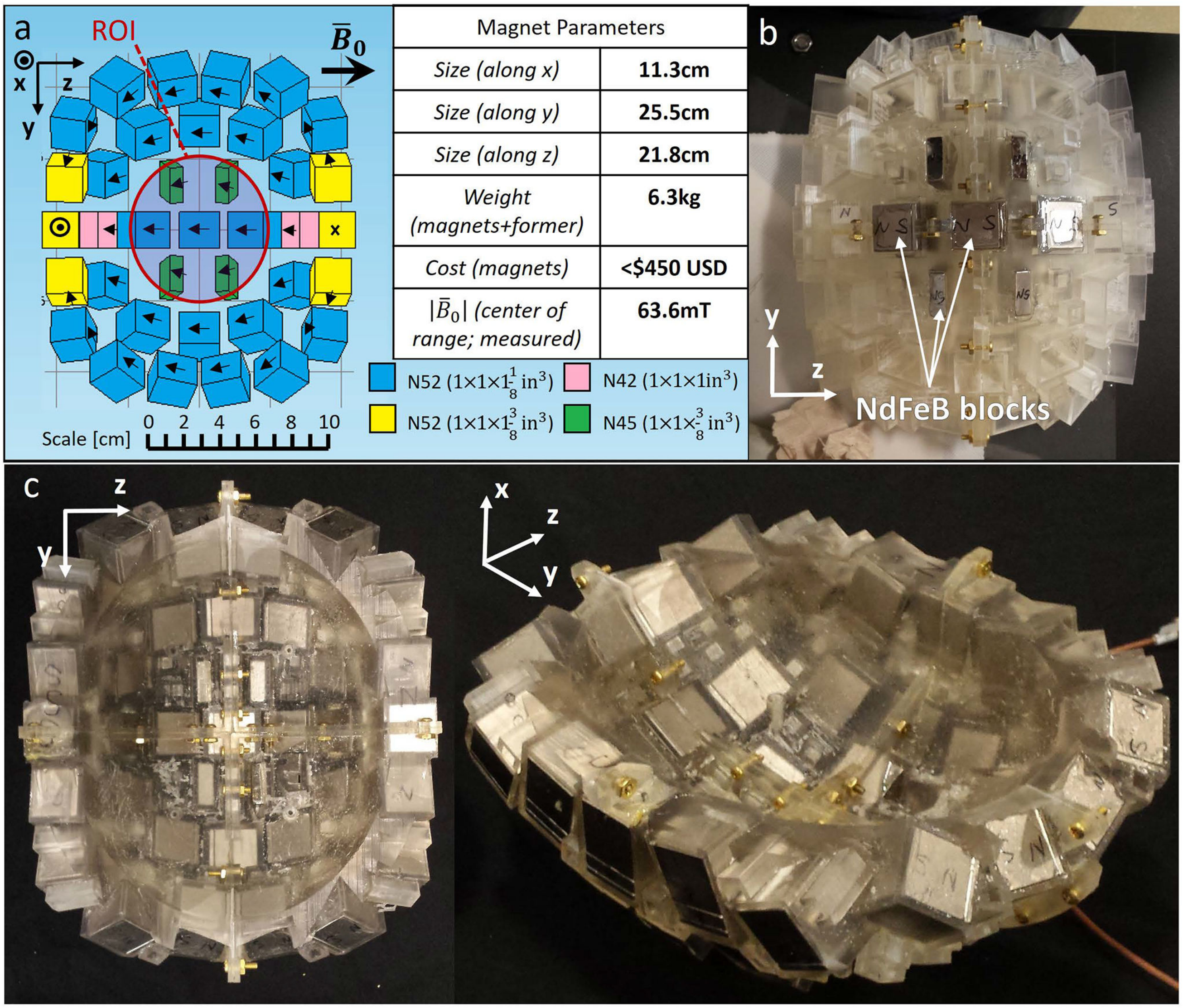

Magnet Parameters	
Size (along x)	**11.3cm**
Size (along y)	**25.5cm**
Size (along z)	**21.8cm**
Weight (magnets+former)	**6.3kg**
Cost (magnets)	**<$450 USD**
$\lvert\bar{B}_0\rvert$ *(center of range; measured)*	**63.6mT**

Figure 3:

(a) The optimized magnet design shown as an assembly of standard-size and –material NdFeB blocks. (b) 3D-printed magnet former generated from a CAD model of the magnet block array. Each block is inserted into the magnet former and secured with an epoxy resin. (c) Final assembled magnet (YZ-plane and oblique views)

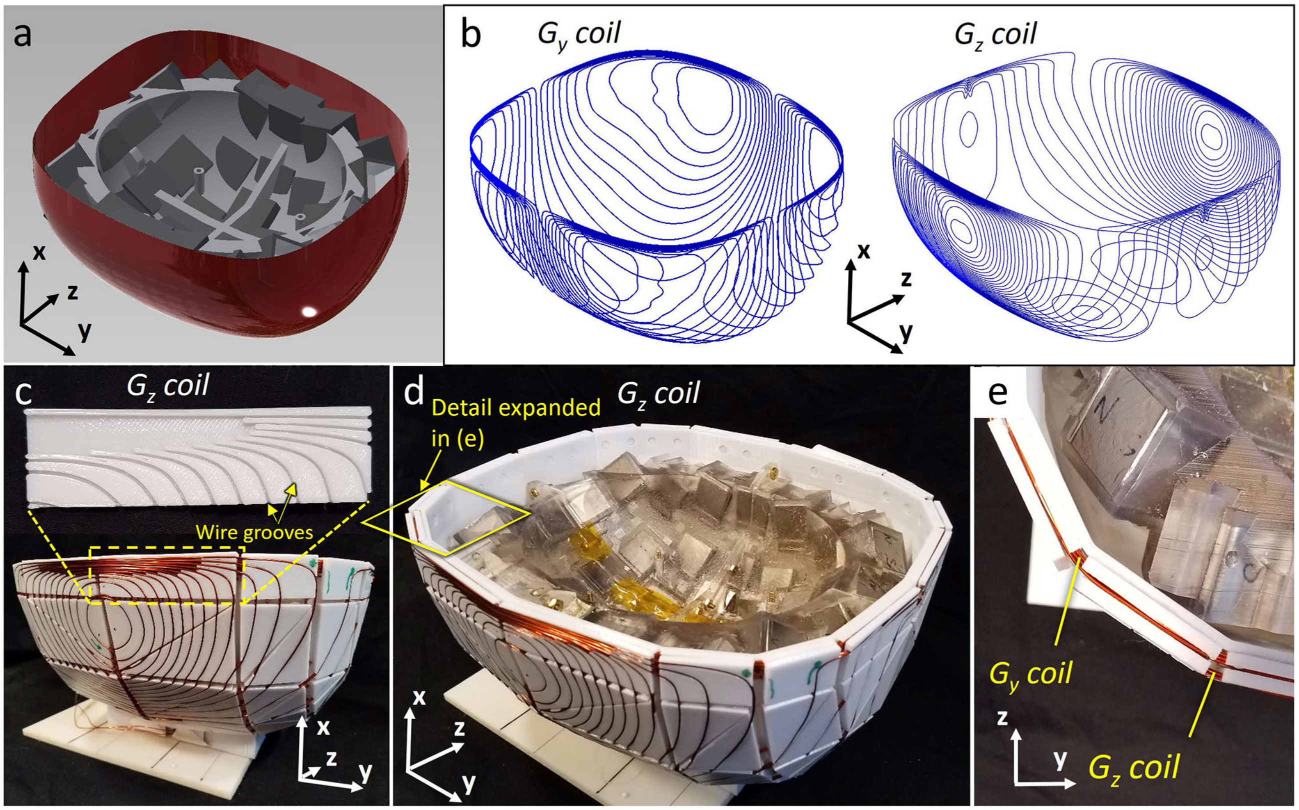

Figure 4:

(a) The red structure shows the surface on which gradient coil stream functions were calculated using a BEM approach. (b) Numerical designs for the G_y (left) and G_z (right) coils. (c) The coil designs are projected onto a piecewise-linear surface. The coil formers are then printed as a series of facets with press-fit wire grooves corresponding to the numerically-derived winding paths. (d) Assembled G_y and G_z coils shown as they are positioned around the B_0 magnet. (e) The G_z coil is constructed immediately atop the G_y coil.

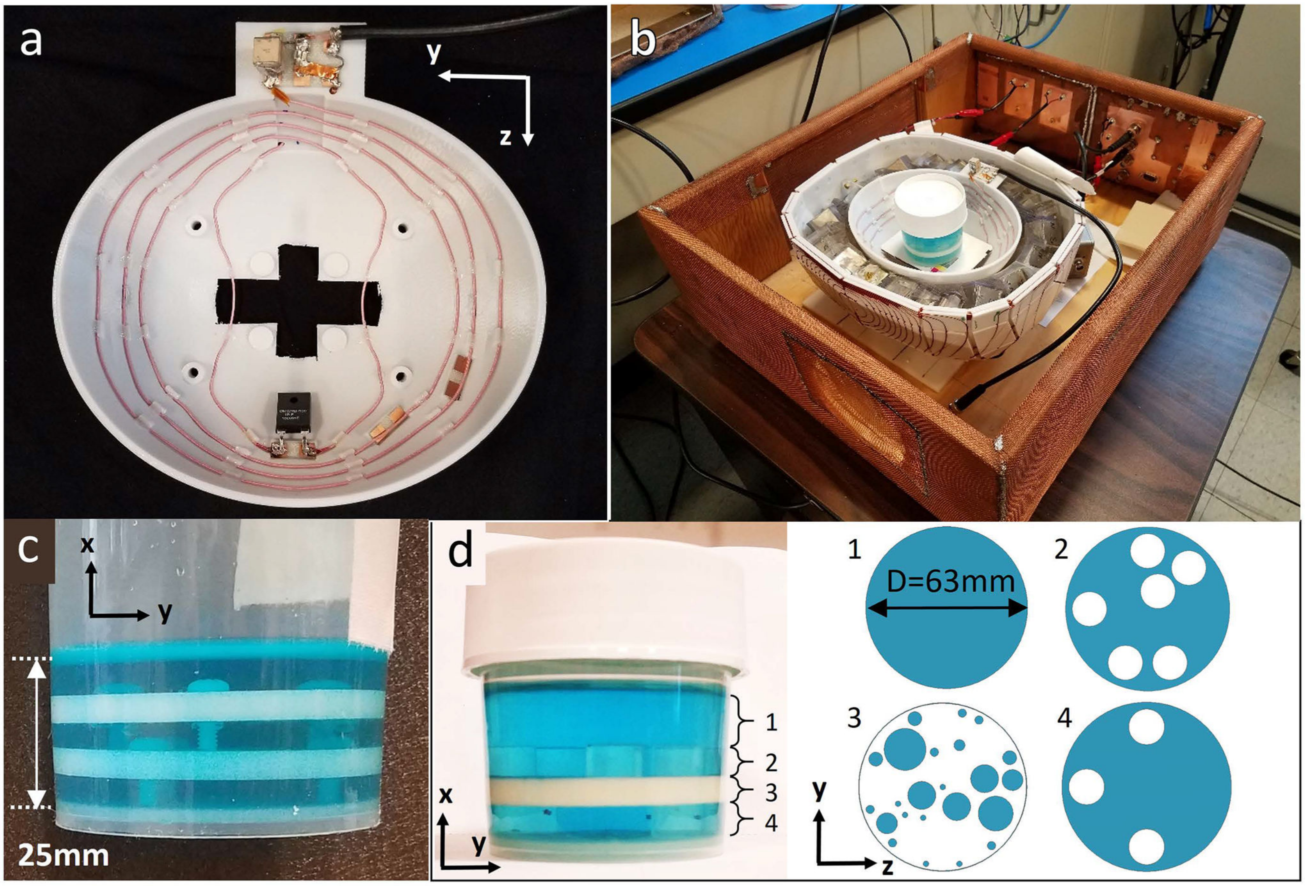

Figure 5:

RF coil and imaging phantoms (a) Volume RF Tx/Rx coil constructed by press-fitting Litz wire into 3D-printed former with numerically-derived grooves. (b) Experimental configuration for 1D and 3D experiments showing the phantom and coil placed inside the magnet/gradient coils, all enclosed in a shielded box (lid removed). (c) Phantom used for 1D depth profiling consisting of 3 × 5mm layers of water with 5mm layers of plastic spaced between. (d) Imaging phantom used for 3D imaging experiments comprised of 4 layers corresponding to different structures placed inside a water bottle.

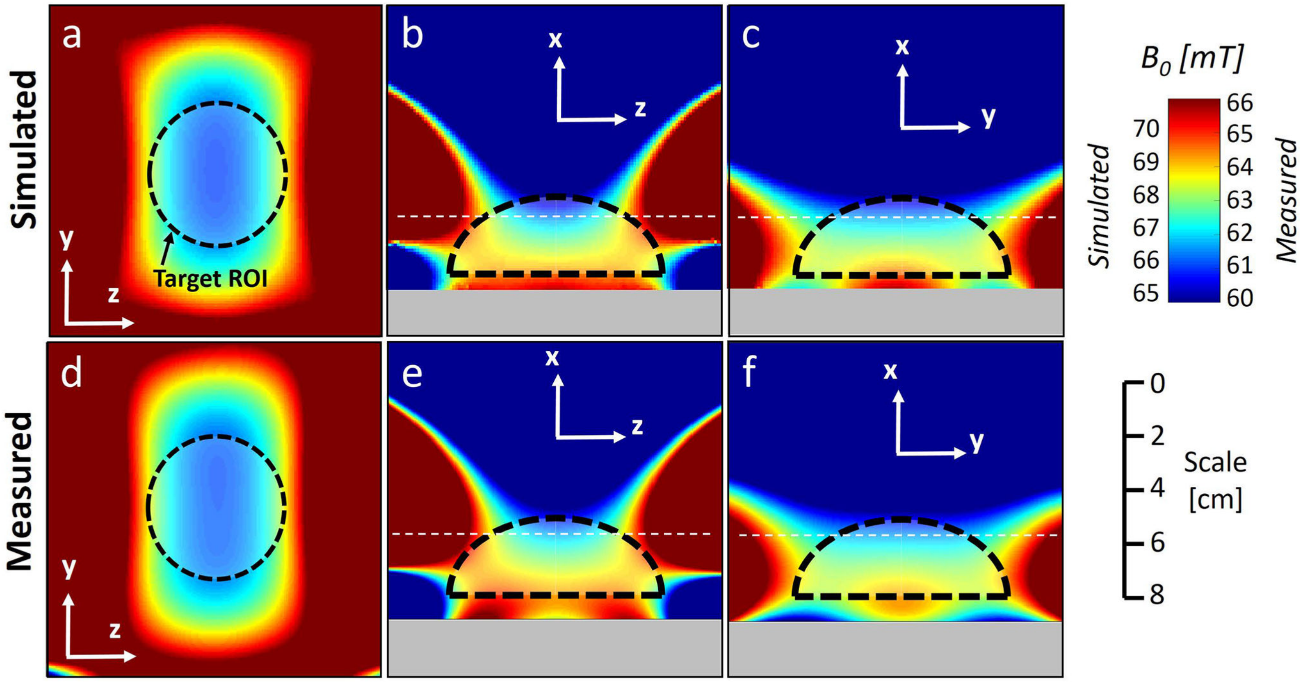

Figure 6:

Simulated and measured B_0 field maps scaled so the ROI mean has identical color. (a) Simulated field map; YZ-plane. (b) Simulated field map; XZ-plane. (c) Simulated field map; XY-plane. (d) Measured field map; YZ-plane. (e) Measured field map; XZ-plane. (f) Measured field map; XY-plane. The black dashed curve marks the design ROI; the gray dashed line indicates the location of the YZ plane in (a) and (d).

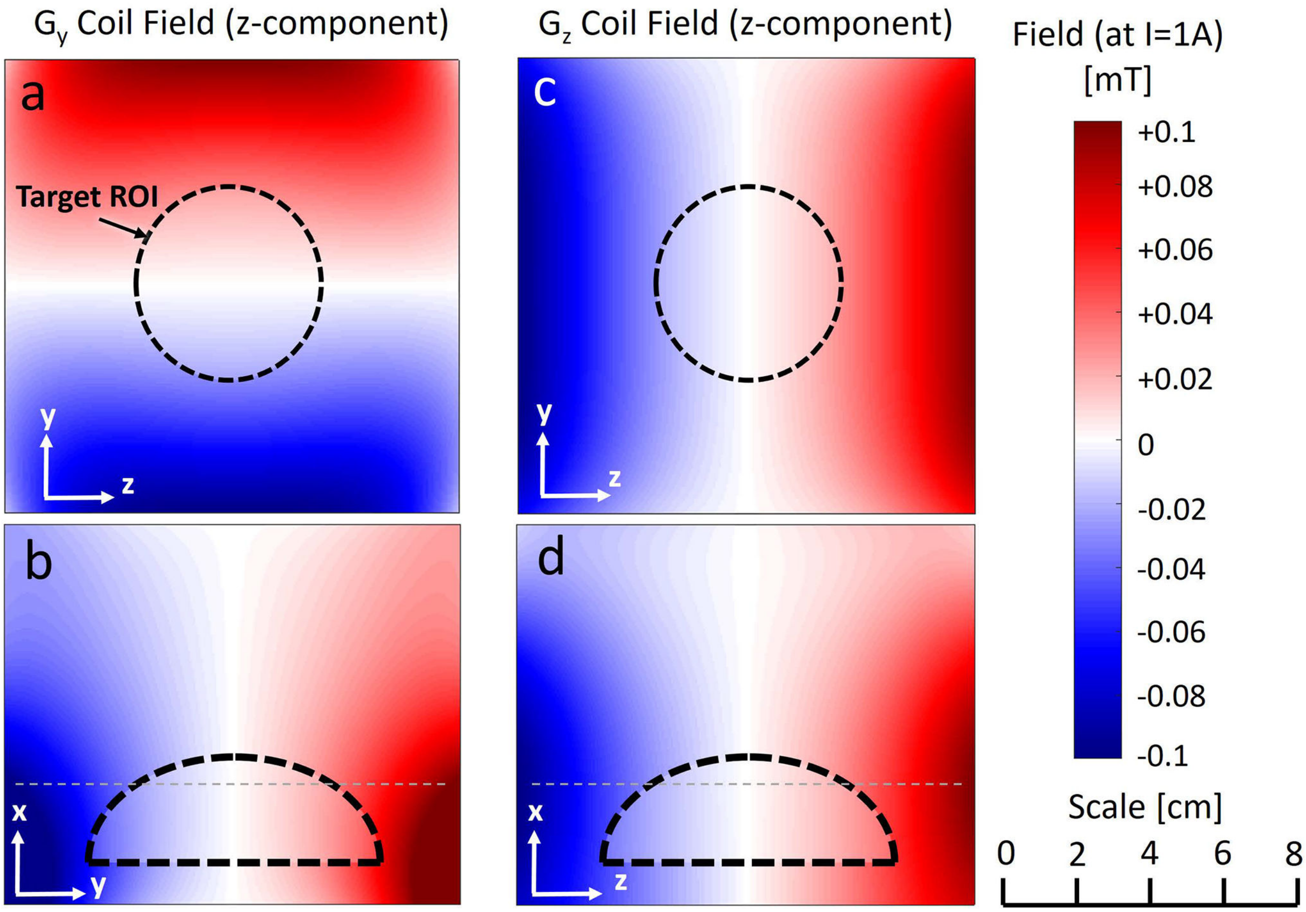

Figure 7:

Gradient coil field maps measured with I=1A. The black dashed curve shows the design ROI; the gray dashed line indicates the location of the YZ plane in (a) and (c). (a) G_y coil; YZ plane. (b) G_y coil; XY plane. (c) G_z coil; YZ plane. (d) G_z coil; XZ plane.

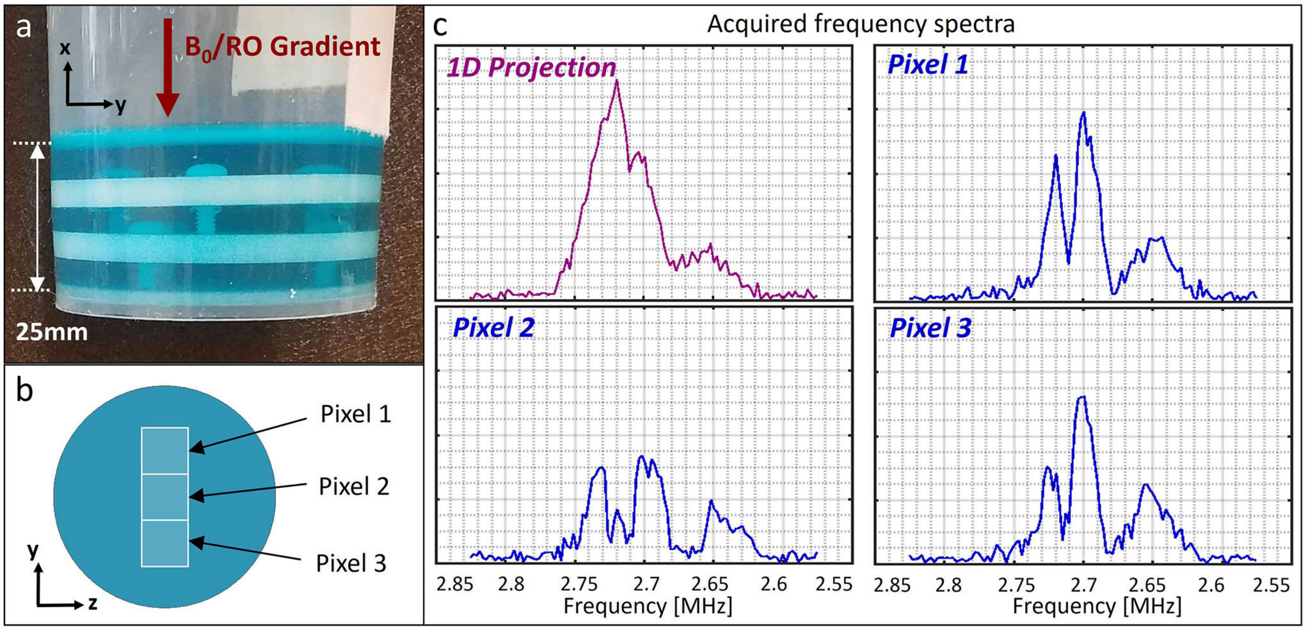

Figure 8:

1D depth profiling results for the 3-layer phantom. (a) Phantom and built-in B_0/readout (RO) gradient direction. (b) Depiction of the 3 phase-encoded pixels (~14×14mm^2) in the YZ plane. (c) Frequency spectra from the non-phase encoded acquisition (projecting over the whole phantom) and each of the three pixels.

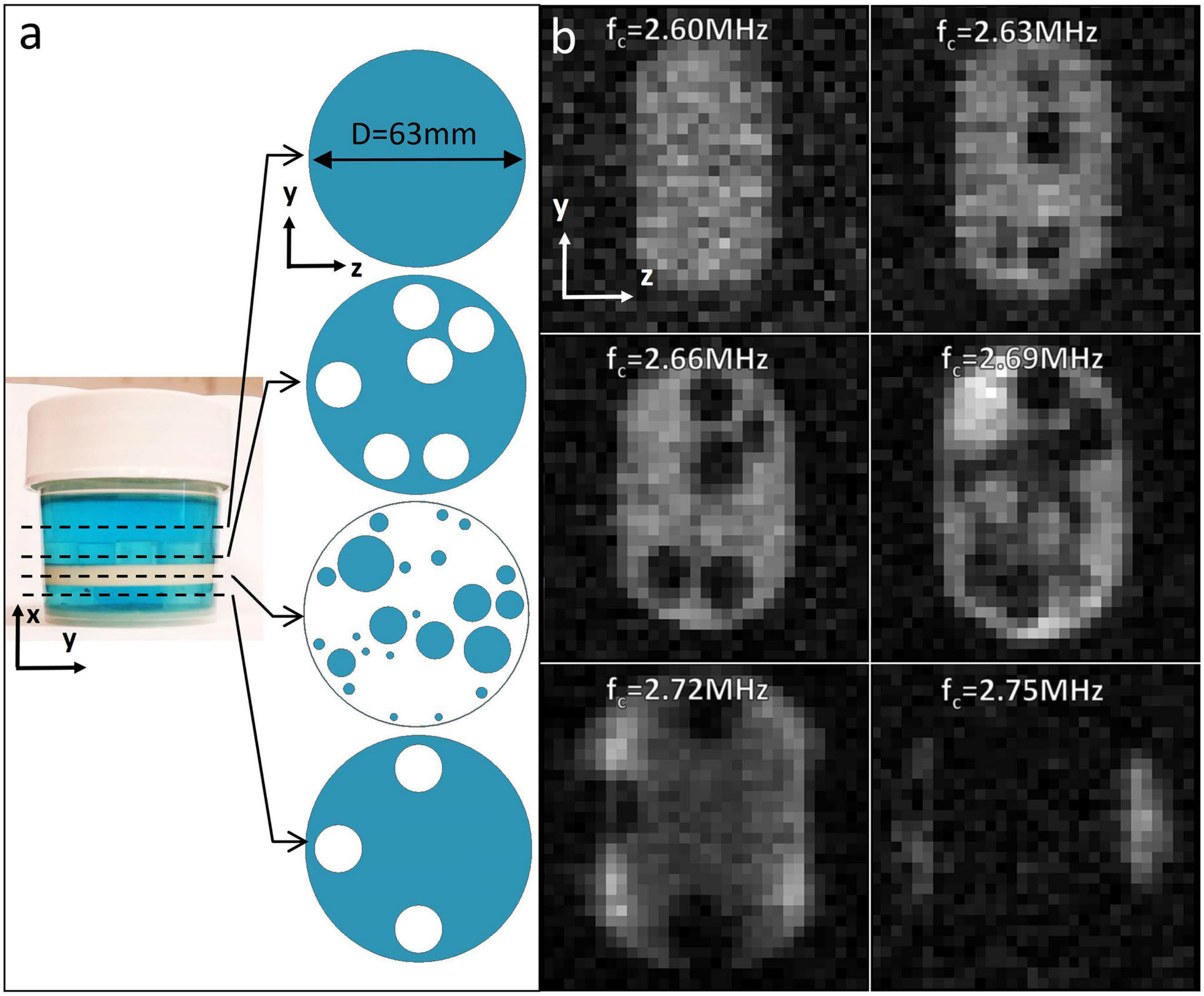

Figure 9:

(a) Imaging phantom for multislice experiments showing YZ-plane structure at different depths. (b) 3D imaging results from the 6 slices acquired using the multislice imaging sequence. Image intensities are scaled to normalize contrast between slices.

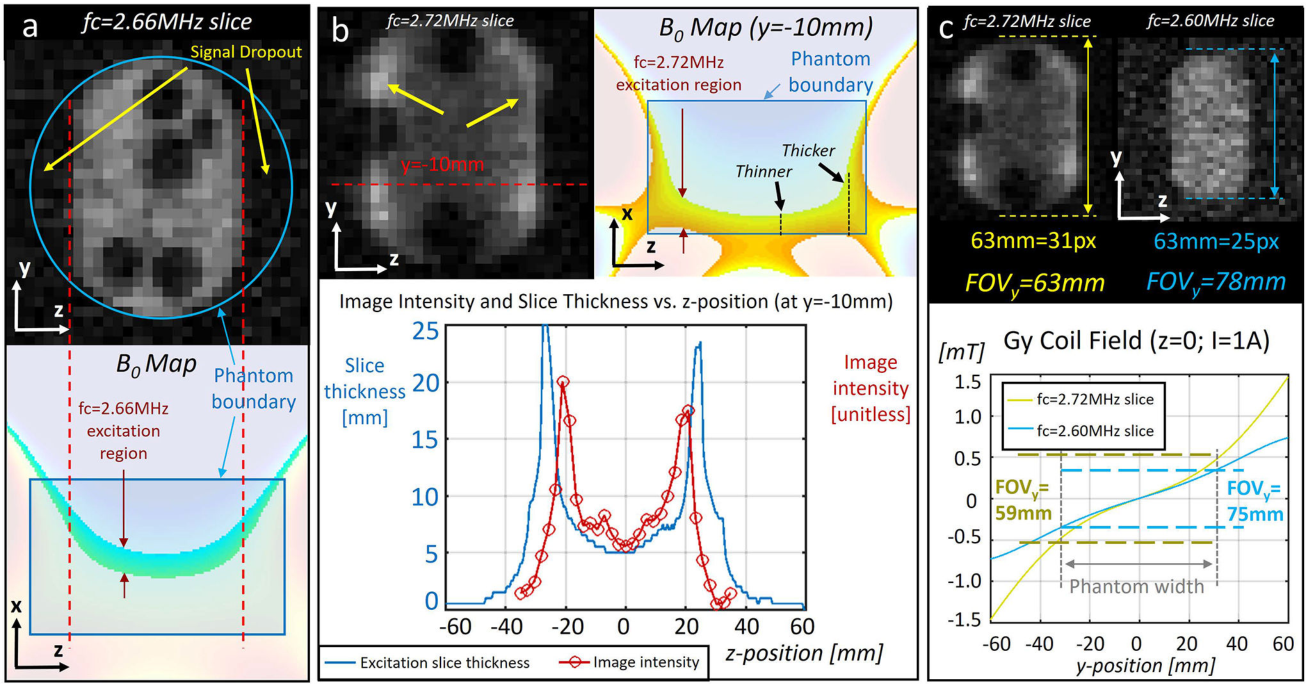

Figure 10:

Analysis of slice curvature and image intensity variations (a) The f_c=2.60MHz slice showing reduced z-extent of the sensitive region. Regions of signal dropout (yellow arrows) correspond to regions of the excitation slice where the isochromats start to curve up along x and become thinner. (b) The f_c=2.72MHz slice contains hyperintense regions (yellow arrows). Visually, these hyperintense regions correspond to the thicker parts of the excitation slice. The plot shows the measured image intensity profile and slice thickness as a function of z position at y=−10mm. (c) The image phantom spans for pixels along the y-dimension in the f_c=2.72MHz slice than in the f_c=2.60MHz slice. From the known size of this phantom and these pixel extents, we can calculate an effective FOV_y for each slice. These measured FOV_y values differ from those expected based on the G_y coil field map and known acquisition parameters by 6.3% and 3.9% for the 2.72MHz and 2.60MHz slices, respectively.